

# DFIR-DETR: Frequency Domain Enhancement and Dynamic Feature Aggregation for Cross-Scene Small Object Detection

Bo Gao, Jingcheng Tong, Xingsheng Chen, Han Yu, and Zichen Li

**Abstract**—Detecting small objects in UAV remote sensing images and identifying surface defects in industrial inspection remain difficult tasks. These applications face common obstacles: features are sparse and weak, backgrounds are cluttered, and object scales vary dramatically. Current transformer-based detectors, while powerful, struggle with three critical issues. First, features degrade severely as networks downsample progressively. Second, spatial convolutions cannot capture long-range dependencies effectively. Third, standard upsampling methods inflate feature maps unnecessarily.

We introduce DFIR-DETR to tackle these problems through dynamic feature aggregation combined with frequency-domain processing. Our architecture builds on three novel components. The DCFNA module uses dynamic K-sparse attention, cutting complexity from  $\mathcal{O}(N^2)$  down to  $\mathcal{O}(NK)$ , and employs spatial gated linear units for better nonlinear modeling. The DFPN module applies amplitude-normalized upsampling to prevent feature inflation and uses dual-path shuffle convolution to retain spatial details across scales. The FIRC3 module operates in the frequency domain, achieving global receptive fields without sacrificing efficiency.

We tested our method extensively on NEU-DET and VisDrone datasets. Results show mAP50 scores of 92.9% and 51.6% respectively—both state-of-the-art. The model stays lightweight with just 11.7M parameters and 41.2 GFLOPs. Strong performance across two very different domains confirms that DFIR-DETR generalizes well and works effectively in resource-limited settings for cross-scene small object detection.

**Index Terms**—Small object detection, frequency domain enhancement, dynamic feature aggregation, cross-scene detection, real-time detection, UAV remote sensing, surface defect inspection

## I. INTRODUCTION

**S**MALL object detection poses unique challenges whether we’re analyzing UAV imagery from hundreds of meters up or inspecting steel surfaces for microscopic defects. These two domains—aerial remote sensing and industrial quality control—couldn’t be more different in their imaging conditions. Yet they share fundamental difficulties that make detection hard. Recent surveys document how UAV systems are transforming precision agriculture, infrastructure monitoring, traffic analysis, and environmental assessment [1]–[3]. Meanwhile, automated inspection has become essential in steel manufacturing, where even tiny surface flaws can compromise product integrity [4]. Both need to find small targets buried in complex backgrounds at various scales.

IoT deployment has made real-time visual inspection critical in these fields. UAV operate as mobile sensing nodes, processing aerial footage on the fly to spot small objects for environmental tracking and infrastructure checks [5]. Factory floors demand defect detection systems that catch subtle surface anomalies as products move through manufacturing

lines [6]. When computer vision meets IoT infrastructure, we need methods that hit high accuracy marks while running fast enough for practical use.

Object detection has changed greatly from hand-designed features to advanced deep models. The Initial approaches based on the histogram of oriented gradients with support vector machine reached their limits as scenes became complex [7]. Convolutional networks changed everything. Two-stage detectors such as Faster R-CNN [8] frame the base of region-based methods. Later, one-stage methods such as YOLO and RetinaNet achieved better speed-accuracy trade-offs by means of anchor-based predictions [9]. DETR [10] re-bracketed detection as set prediction and dropped hand-engineered components altogether. RT-DETR [11] further advanced with an efficient hybrid encoder that decouples intra-scale interaction and cross-scale fusion, achieving same speed as YOLO while enjoying end-to-end training.

Progress hasn’t solved everything though. The small object detection in various situations is still a challenging task. Below  $32 \times 32$  pixels, objects lose key features as they are downsampled by networks [12]. Low resolution means that there’s not enough detail to draw accurate boxes and labels. Classic spatial convolutions have rather small receptive fields—they lack a long range context required to separate small objects from cluttered background [13]. The feature pyramid is usually based on simple nearest-neighbor upsampling, which introduces artifacts and brings large inflation in the number of channels, suffering from poor representations for small targets. While most detectors pool features statically with a fixed receptive field, and do not perform well when object scales change dramatically over the scenes [14]. High frequency patterns, which are important for exact boundaries and delicate defect, are lost during conventional feature extraction [15].

We propose DFIR-DETR to address these limitations head-on. Our architecture merges dynamic feature aggregation with frequency-domain enhancements. Beyond the architecture itself, we establish theoretical grounding for frequency-domain operations in detection transformers. Formal complexity analysis proves the computational gains from dynamic sparse attention. We derive convergence bounds for frequency-domain iterative refinement. Signal processing theory tells us small objects appear as high-frequency components in the spatial-frequency spectrum—this motivates our frequency-domain operations for preserving edge details. Fourier transforms enable global receptive fields at  $\mathcal{O}(N \log N)$  complexity versus  $\mathcal{O}(N^2)$  for standard self-attention. We also provide information-theoretic justification: mutual information between queries and keys follows power-law distribution, making  $K$ -sparse approximation possible with bounded error.

Our contributions are organized into three parts. First, spatial gated linear units enhance nonlinear modeling and decrease computational cost from  $\mathcal{O}(N^2)$  to  $\mathcal{O}(NK)$  via a dynamic K-sparse attention. Second, DFPN takes amplitude-normalized upsampling to constrain feature map expansion and dual-path shuffle convolution for effective multi-scale spatial information preservation together. Third, FIRCD3 reconstructs the feature pooling in frequency domain that can learn global receptive fields more efficiently. Conclusion DFIR-DETR clearly has a solid generalization in the detection of different situations with optimal on-line performance

## II. RELATED WORK

### A. Object Detection Algorithms

Deep learning has reshaped object detection over the past decade, though the field's evolution reveals persistent trade-offs between speed and precision. Detectors broadly split into two camps: two-stage methods that carefully scrutinize candidate regions, and one-stage approaches that predict directly from image grids.

Two-stage detectors originate from R-CNN [16], where Girshick et al. were jointly learned based on region proposals and CNN activations. Although showing strong innovation, this pipeline was computationally redundant, and we had to compute features multiple times for overlapping regions. Faster R-CNN [17] has overcome the problem by designing the Region Proposal Network (RPN) with a shared convolutional feature between proposal and classification. Such architectural intuition that proposal and detection can share the same feature maps was critical. The RPN eliminated the selective search overhead, and end-to-end training became possible on the whole system, but its two-stage nature still arguable due to the fact that it had two separate inference steps for new region proposals and detection.

One-stage detectors took a very different path, just eliminating region proposals all together. Liu et al.'s SSD [18] discretizes the detection process by priors being placed on several feature maps, and treats the detection as a dense prediction assignment for multiple scales. Redmon et al. generalized the idea with YOLO [19] which reincarnates detection into a pure regression task: it partitions the image into grids and then predicts boxes and classes simultaneously. While this extreme simplification enabled real-time inference, it initially lagged in precision when capturing small or overlapping objects. This gap was later reduced by YOLOv3 [20] using multi-scale predictions and deeper backbone, indicating one-stage method could approach two-stage performance without the high computation cost. However, the most recent versions of YOLO do not generalize to the small object detection problem we consider in this work.

Transformers disrupted this landscape recently. DETR Carion et al. eliminated hand-crafted modules such as NMS and anchor boxes by set-based prediction with bipartite matching loss. This complexity comes at a price—vanilla DETR is slow to train and requires a considerable amount of computation, which makes it infeasible for real-time deployment.

### B. RT-DETR Framework

RT-DETR bridges the gap between theoretical advance of transformer and its utilitarian usage. The architecture can be decomposed into three components: a CNN backbone for multi level feature representation; a hybrid encoder with attention and convolution mixed for multi scale feature fusion; and a transformer decoder that iteratively refines the query.

The backbone is ResNet [21] or other CNN networks that can extract features from different scales. RT-DETR, in contrast, directly activates all last three backend stages possible of a richer multi-scale hierarchy. This is particularly important for objects that cover many orders of magnitude in scale from pedestrians the size of patches of pixels in drone imagery, to full-size vehicles which dominate the frame.

The encoder, which is the crux of RT-DETR's novelty. Instead of performing full self-attention at all scales that would be prohibitively expensive, it divides operations in two modules. Attention-based Intra-scale Feature Interaction (AIFI) and CNN-based Cross-scale Feature Fusion (CCFF) build upon self-attention to perceive long-range dependencies in each scale, and operate efficient convolutions for information across scales respectively. The hybrid design is motivated by an observation: within-scale modeling could benefit from attention's global receptive field, while cross-scale fusion might also be well-served by the convolutional inductive biases about spatial hierarchy.

The decoder also iteratively updates the object queries through cross-attention mechanism with the encoder features. RT-DETR provides query selection that minimizes uncertainty queries seeded from the most confident encoder features, rather than learned embeddings. This allows convergence to be much faster, as the training process of vanilla DETR is rather slow. The decoder also provides trade-offs between efficiency and accuracy, as the number of layers can be manipulated at inference time without retraining, but these trade-offs are not highly tunable when architectural changes need to highlight a specific set of detection scenarios.

### C. Feature Extraction and Feature Fusion Networks

Multi-scale feature handling separates good detectors from great ones, especially for small objects where resolution loss proves catastrophic. Research has pursued two parallel threads: enhancing feature extraction's adaptivity and optimizing multi-scale fusion topology.

Deformable Convolutional Networks [22] by Dai et al. tackled the first challenge by adding learnable offsets to standard convolutions. Instead of sampling from fixed grid locations, deformable convolutions learn where to sample based on content. This matters for objects with irregular shapes or scales—the network adapts its receptive field geometry rather than forcing all objects through the same fixed sampling pattern. However, deformable convolutions alone don't address how to fuse information across scales.

Feature Pyramid Networks (FPN) [23] established the dominant fusion paradigm. Lin et al. combined top-down semantic propagation with lateral connections, creating pyramids where every level has strong semantics and appropriate resolution

for its scale. The key insight: high-level features carry semantic meaning but lack spatial precision, while low-level features have sharp resolution but weak semantics. FPN's lateral connections merge these complementary properties. Still, information flows primarily top-down, which may not optimally serve all objects.

PANet [24] by Liu et al. questioned this unidirectional flow. Adding a bottom-up pathway alongside FPN's top-down structure, PANet creates bidirectional information flow. This shortens paths between low-level localization details and high-level semantics, helping both small objects that need precise boundaries and large objects that need broad context. PANet's adaptive feature pooling further allows each region proposal to aggregate features from all pyramid levels rather than being assigned to a single scale, though this flexibility increases computational cost.

EfficientDet [25] by Tan et al. optimized fusion efficiency through BiFPN, which prunes single-input nodes (contributing nothing to fusion) and adds cross-scale skip connections. Learnable weights let the network emphasize important features dynamically. This proved especially effective when combined with compound scaling of backbone, fusion network, and resolution.

NAS-FPN [26] took automation further—Ghiasi et al. used neural architecture search to discover fusion topologies automatically rather than hand-designing them. The search space includes all possible connections between pyramid levels. While NAS-FPN found novel architectures outperforming hand-crafted designs, search cost remains high and the resulting architectures can be irregular, complicating deployment.

These fusion networks have the limitation our work overcomes: they are spatial-based without any design for cross-scale connection except upsampling and convolution. None of them use frequency-domain features even though the signal-processing theory strongly advocates that small objects concentrate energy in the high-frequency components. This spatial-only attention is the reason we derive frequency-domain methods.

### III. METHODS

Addressing the dual challenges of small object detection in unmanned aerial vehicle (UAV) remote sensing scenarios and steel surface defect identification in industrial contexts, we present an enhanced real-time detection architecture. As illustrated in Fig. 1, the proposed network incorporates three synergistic optimization modules to tackle the sparse feature representation of distant small-scale objects in the VisDrone dataset and the difficulty of capturing subtle defect textures in the NEU-DET dataset. Specifically, the DCFA module integrated into the Backbone network leverages dynamic K-sparse attention mechanisms to achieve adaptive focus on defect regions and small targets. Within the Neck network, DFPN suppresses feature inflation through amplitude-normalized upsampling while preserving multi-scale spatial details via dual-path shuffle convolution. The FIRC3 module in the feature fusion layer establishes global receptive fields in the frequency domain, effectively capturing long-range dependencies. This

architecture demonstrates superior generalization capability across diverse detection scenarios, substantially improving detection precision for minute objects while maintaining real-time performance.

#### A. DCFA

The Backbone Architecture of conventional RT-DETR structure would face a great difficulty in handling object detection tasks under complex scenes. The original ResNet-based Backbone adopts homogeneous BasicBlock modules in the entire networks, it has inherent three drawbacks. First, stacking down-sampling operations restricts the representation ability of the net work for small-scale objects and subtle defect features in deeper layers, meanwhile can not effectively retain redundant geometry information and edge detail. Second, the predetermined receptive field expansion manner is lack of flexibility in accommodating multi-scale object distributions from sub-pixel level anomalies to large-scale backgrounds. Third, due to the lack of explicit spatial attention mechanisms, when the network is exposed to dense scenes and high complexity background interference, target regions cannot be effectively focused on by the network which cause false positive rate and false negative rate persistently remain high. To overcome these bottlenecks, we propose the DCFA module, which integrates adaptive spatial attention through DKSA (dynamic K-sparse attention), enhanced nonlinear modeling capability via SGLU (spatial gated linear units), and multi-scale residual fusion paths. This design maximally preserves shallow geometric and texture details while maintaining deep semantic information. As illustrated in Fig. 2

The DCFA module adopts a cross-stage partial (CSP) network architecture, achieving gradient-efficient propagation and multi-scale feature fusion through dual-path feature flows. The complete feature transformation process can be mathematically formulated as:

$$Y = \phi_{cv2} \left( \text{Concat} \left[ F_1, F_2, G_1(F_2), G_2(G_1(F_2)), \dots, G_n(G_{n-1}(\dots)) \right] \right) \quad (1)$$

$$[F_1, F_2] = \text{split} (\phi_{cv1}(X)) \quad (2)$$

where  $G_i$  represents the  $i$ -th DAFB (Dynamic Attention Fusion Block) transformation operator,  $n$  denotes the stacking depth, and  $\phi_{cv1}$  and  $\phi_{cv2}$  represent the input and output  $1 \times 1$  convolutional projection layers, respectively.

DAFB achieves comprehensive feature enhancement by cascading three functionally complementary sub-modules. Its forward propagation follows the transformation chain:

$$Z = \text{SGLU}(H + \text{DKSA}(H)), \quad H = X + \phi_{dw}(X) \quad (3)$$

where  $\phi_{dw}$  denotes a  $3 \times 3$  depthwise separable convolution with batch normalization. The DKSA mechanism subsequently operates on the enhanced features  $H$ , selectively focusing on defect regions in industrial scenarios through dynamic sparsification strategies while establishing long-range associations between small objects and contexts in remote sensing

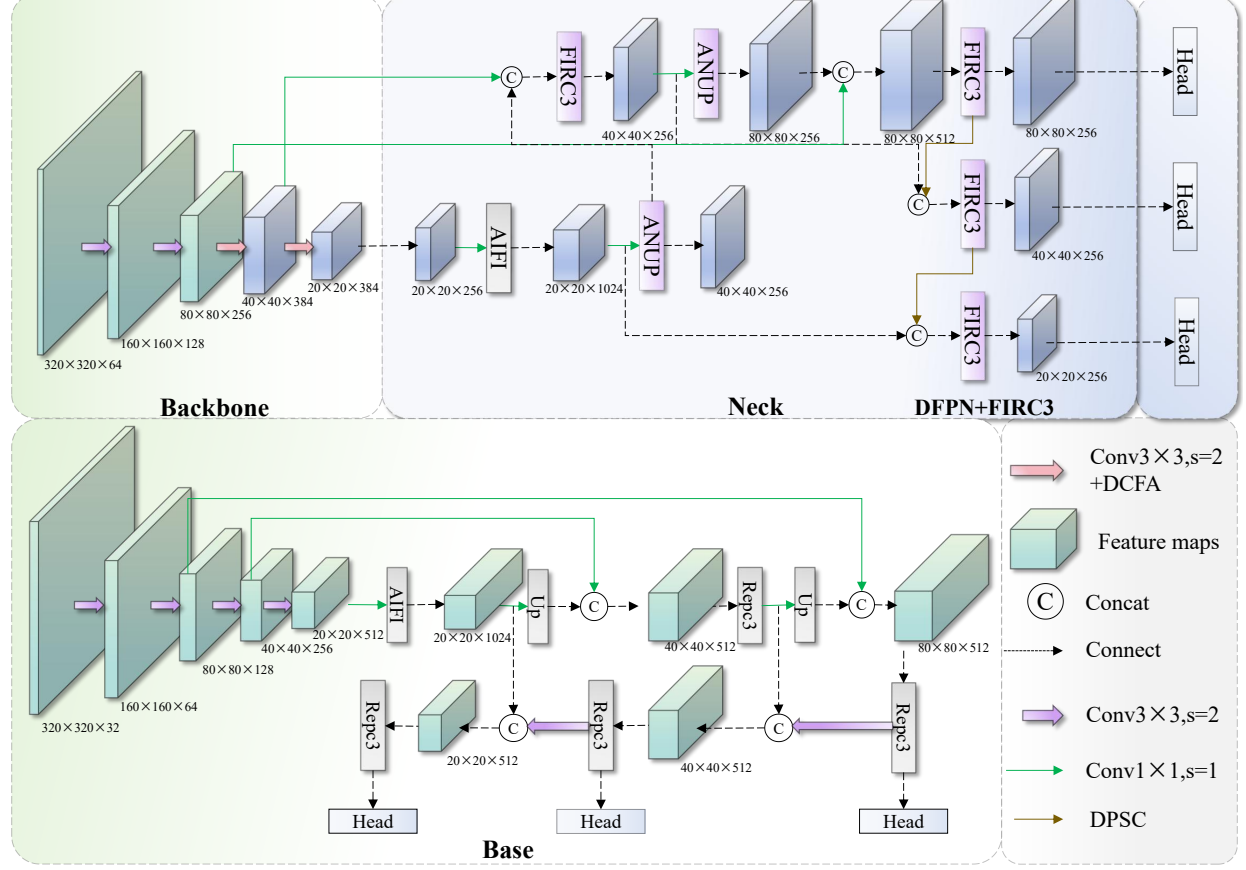


Fig. 1: Overall architecture of DFIR-DETR.

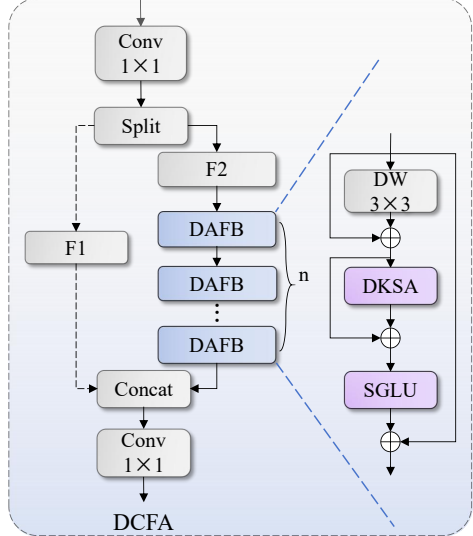


Fig. 2: DCFA block

$$SGLU(X) = X + \phi_{out} \left( \mathcal{D} \left( \left( \phi_{act} \left( \phi_{dw}^{3 \times 3} (X_g) \right) \right) \odot X_v \right) \right) \quad (4)$$

$\phi_{dw}^{3 \times 3}$  represents the  $3 \times 3$  depthwise convolution applied to the gating stream, encoding local spatial contextual information into gating signals so that gating decisions integrate neighborhood spatial patterns rather than relying solely on single-point feature values.  $\phi_{act}$  employs the GELU activation function, providing smoother gradient flow compared to ReLU. Element-wise multiplication  $\odot$  implements gating modulation, and  $\mathcal{D}$  denotes Dropout regularization.

DKSA implements computationally efficient self-attention through a dynamic Top-K selection strategy, demonstrating excellent adaptability in both industrial defect detection and remote sensing small object recognition scenarios. As illustrated in Fig. 3. Combined with LGN (Layer Group Normalization) preprocessing, the complete attention computation process can be uniformly expressed as:

$$DKSA(X) = \phi_{proj} \left( \text{Concat} \left[ (VA^T)^{reshape}, X_2 \right] \right) \quad (5)$$

$$A_{ij} = \begin{cases} \frac{\exp(s_{ij})}{\sum_{j' \in \mathcal{T}_K^i} \exp(s_{ij'})}, & j \in \mathcal{T}_K^i \\ 0, & j \notin \mathcal{T}_K^i \end{cases} \quad (6)$$

scenarios. SGLU (Spatial Gated Linear Unit) serves as a feedforward network to perform nonlinear transformation and channel mixing on attention-enhanced features. Its gating mechanism adaptively modulates the activation intensity of different channels, further improving cross-scene feature discriminability. The mathematical expression is:

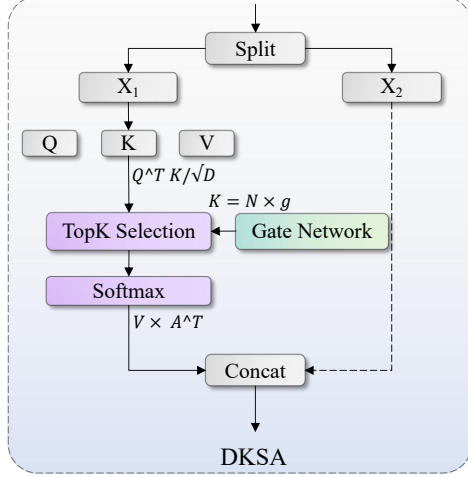


Fig. 3: DKSA block

**Algorithm 1** DCFA

**Require:** Input feature map  $X \in \mathbb{R}^{C \times H \times W}$ , stack depth  $N$   
**Ensure:** Enhanced feature map  $Y \in \mathbb{R}^{C \times H \times W}$

- 1:  $X_1, X_2 \leftarrow \text{Split}(X)$  // Dual-path feature flow
- 2:  $F \leftarrow X_1$
- 3: **for**  $i = 1$  **to**  $N$  **do**
- 4:   // Dynamic Attention Fusion Block
- 5:    $F' \leftarrow \text{DWConv}_{3 \times 3}(F) + \text{BN}(F)$
- 6:   // Dynamic K-Sparse Attention
- 7:    $F'' \leftarrow \text{LGN}(F')$
- 8:    $Q, K, V \leftarrow \text{Linear}(F'')$
- 9:    $\rho \leftarrow \sigma(\text{Gate}(F''))$
- 10:    $k \leftarrow \lfloor \rho \cdot HW \rfloor$
- 11:   **for each** position  $j$  **in**  $[1, HW]$  **do**
- 12:      $\mathcal{I}_k^j \leftarrow \text{TopK}(Q_j \cdot K^T, k)$
- 13:      $\text{Attn}_j \leftarrow \text{Softmax} \left( \frac{Q_j \cdot K_{\mathcal{I}_k^j}^T}{\sqrt{d}} \right) \cdot V_{\mathcal{I}_k^j}$
- 14:   **end for**
- 15:   // Spatial Gated Linear Unit
- 16:    $G \leftarrow \text{GELU}(\text{DWConv}_{3 \times 3}(\text{Attn}))$
- 17:    $F \leftarrow \text{Dropout}(\text{Linear}(\text{Attn}) \odot G)$
- 18: **end for**
- 19:  $Y \leftarrow \text{Conv}_{1 \times 1}(\text{Concat}(F, X_2))$
- 20: **return**  $Y$

The dynamic Top-K selection mechanism is defined as:

$$K = \lfloor N \cdot \sigma(\text{AvgPool}(\psi(X))) \rfloor \quad (7)$$

where  $\psi$  represents a gating network composed of two convolutional layers,  $\sigma$  denotes the sigmoid function, and the output scalar value determines the proportion of attention connections to retain.  $\mathcal{I}_K^i = \text{TopK}(S_i, K)$  returns the index set of the top  $K$  most relevant key positions for the  $i$ -th query position. Unselected connections are masked to zero, thereby converting the attention matrix from dense to structurally sparse, reducing computational complexity from  $\mathcal{O}(N^2)$  to  $\mathcal{O}(NK)$ .

The DCFA module fundamentally enhances RT-DETR's performance in cross-scene object detection scenario through

multi-dimensional collaborative optimization. The dynamic K-sparse attention pruning mechanism enables content-adaptive allocation of computational resources, focusing more attention connections on defect regions in industrial scenarios to capture subtle textures while performing aggressive pruning on uniform backgrounds to reduce redundancy. In remote sensing scenarios, it allocates sufficient contextual modeling capability to small objects while sparsifying large irrelevant backgrounds, achieving optimal trade-offs between accuracy and efficiency in both scenarios. The spatial gated linear unit provides nonlinear modeling capability far exceeding traditional ReLU through spatialized gating signals. Its smooth gradient characteristics avoid gradient vanishing problems, enabling stable training of deep networks and learning of more refined feature transformations. The effectiveness of dynamic  $K$ -selection can be understood through rank approximation theory. For natural image features, the attention matrix exhibits rapid singular value decay following power-law distribution. The approximation error decreases exponentially with  $K$ , providing quantitative trade-offs between computational budget and detection accuracy. The learnable gating mechanism in Eq. (7) adaptively determines  $K$  based on local feature statistics, which can be interpreted as solving an optimization problem that balances detection reward against computational cost. This enables the network to automatically adjust the trade-off between efficiency and accuracy for each input sample based on scene complexity.

**B. DFPN**

The cross-scale feature fusion module CCFF in conventional RT-DETR relies on simple nearest neighbor upsampling and direct concatenation operations for multi-scale feature integration. However, abrupt transitions between feature scales introduce semantic discontinuities, compromising feature representation quality with particularly significant impact on small objects where spatial resolution is critical. Original upsampling operations generate redundant high-frequency artifacts in the absence of proper normalization, leading to feature map inflation and reduced computational efficiency. The symmetric top-down pathway lacks sufficient consideration of information density differences between scales, resulting in suboptimal feature fusion performance in small object detection tasks. To address these fundamental deficiencies of CCFF, we propose the DFPN, a novel Neck architecture that integrates ANUP (Amplitude Normalized Upsampling) modules in the top-down pathway DPSC (Dual-path Shuffle Convolution) blocks in the bottom-up pathway. As illustrated in Fig. 4, DFPN effectively mitigates feature map inflation through adaptive amplitude normalization and preserves fine-grained spatial details through dual-path convolution operations, establishing more coherent cross-scale feature representations and significantly enhancing the model's capability to detect small objects in complex scenarios. DFPN consists of two synergistic components operating on complementary pathways of the feature pyramid. In the top-down pathway, the ANUP module reconstructs traditional upsampling operations by introducing amplitude-dependent normalization factors to compensate for

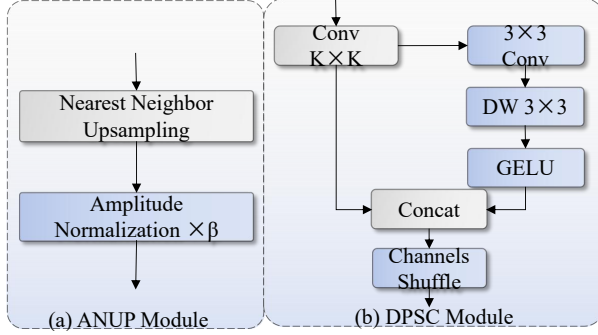


Fig. 4: DFPN block

feature amplitude inflation caused by spatial expansion. Given an input feature map  $F_i$  at scale  $i$ , the ANUP operation produces amplitude-controlled upsampled feature maps:

$$F_i^\uparrow = \beta \cdot \mathcal{U}(F_i) = \frac{1}{s^2} \cdot \mathcal{U}(F_i) \quad (8)$$

where  $\mathcal{U}(\cdot)$  denotes the nearest neighbor upsampling operator with scale factor  $s$ , and  $\beta = 1/s^2$  represents the amplitude normalization coefficient, maintaining consistent feature intensity across different scales. This normalization strategy ensures that upsampled features retain original information density, preventing the feature map inflation common in traditional CCFN upsampling operations. The theoretical foundation stems from the fact that spatial interpolation inherently amplifies the feature map  $L_1$  norm by a factor proportional to the square of the upsampling ratio. The proposed amplitude normalization counteracts this effect by maintaining the relationship:

$$\begin{aligned} \|F_i^\uparrow\|_1 &\approx \|F_i\|_1 \cdot \frac{s^2 \cdot H \cdot W}{H \cdot W} \cdot \frac{1}{s^2} \\ &= \|F_i\|_1 \end{aligned} \quad (9)$$

establishing a more stable feature propagation mechanism, which is particularly significant for preserving subtle appearance features of small objects.

In the bottom-up pathway, the DPSC module addresses information loss during downsampling through a dual-path architecture. The first path performs standard convolution to extract semantic features, while the second path takes the output of the first path as input, capturing spatial details through cascaded convolutions, ultimately fusing dual-path information through channel shuffling. The DPSC operation is formulated as:

$$F_{out} = \mathcal{M} \left( \text{Concat} \left( F_1^{std}, \phi \left( W_d * (W_{conv} * F_1^{std}) \right) \right) \right) \quad (10)$$

$F_1^{std}$  represents semantic features extracted through standard convolution with activation function  $\sigma(\cdot)$ ,  $W_{conv}$  and  $W_d$  denote the  $3 \times 3$  standard convolution kernel and  $3 \times 3$  depthwise convolution kernel (groups=C/2) in the second path respectively,  $\phi(\cdot)$  represents the GELU activation function providing smooth gradient flow, and  $\mathcal{M}(\cdot)$  denotes the channel shuffle operation. The channel shuffle mechanism is mathematically represented as a tensor rearrangement operation:

---

**Algorithm 2** DFPN

---

**Require:** Multi-scale features  $\{F_i\}_{i=1}^L$ , scale  $s$   
**Ensure:** Enhanced features  $\{F_i^{\text{out}}\}_{i=1}^L$

- 1:  $F_L^{\text{up}} \leftarrow F_L$
- 2: // **Top-down with ANUP**
- 3: **for**  $i = L - 1$  **down to** 1 **do**
- 4:    $F_i^{\text{up}} \leftarrow \text{ANUP}(F_{i+1}^{\text{up}}, F_i, s)$
- 5: **end for**
- 6: // **Apply DPSC**
- 7: **for**  $i = 1$  **to**  $L$  **do**
- 8:    $F_i^{\text{out}} \leftarrow \text{DPSC}(F_i^{\text{up}})$
- 9: **end for**

10: **Procedure** **ANUP**( $F_{\text{high}}$ ,  $F_{\text{low}}$ ,  $s$ ):  
11:    $F_{\text{up}} \leftarrow \text{Upsample}(F_{\text{high}}, s)$   
12:    $F_{\text{norm}} \leftarrow (1/s^2) \cdot F_{\text{up}} // \text{Amplitude normalization}$   
13:   **return**  $\text{Conv}_{1 \times 1}(\text{Concat}(F_{\text{norm}}, F_{\text{low}}))$

14: **Procedure** **DPSC**( $F$ ):  
15:    $F_1 \leftarrow \sigma(W_{\text{std}} * F) // \text{Path 1}$   
16:    $F_2 \leftarrow \text{GELU}(W_d * \text{GELU}(W_{\text{pw}} * F)) // \text{Path 2}$   
17:   **return**  $\text{ChannelShuffle}(\text{Concat}(F_1, F_2))$

---

$$\mathcal{M}(F) = \text{Reshape} \left( \text{Permute} \left( \text{Reshape}(F, [B, 2, C/2, H, W]), [0, 2, 1, 3, 4] \right), [B, C, H, W] \right) \quad (11)$$

reorganizing feature channels to facilitate cross-path information exchange. The second path in DPSC constitutes a spatial detail capture branch, taking the output  $F_1^{std}$  of the first path as input and achieving fine-grained feature extraction through cascaded convolution operations:

$$F_2^{dep} = \phi \left( W_d * (W_{conv} * F_1^{std}) \right) \quad (12)$$

where  $W_{conv}$  is a  $3 \times 3$  standard convolution kernel for initial spatial feature transformation, and  $W_d$  is a  $3 \times 3$  depthwise convolution kernel for efficient spatial filtering. Through grouped operations, spatial features are progressively refined while maintaining computational efficiency, with GELU activation ensuring smooth gradient propagation required for training stability. The concatenation and shuffling of features from both paths establish comprehensive feature representations, integrating semantic information from the standard convolution path with fine-grained spatial details from the cascaded convolution path. The effective receptive field of DPSC is approximately:

The integration of ANUP and DPSC modules in the DFPN architecture establishes a more sophisticated feature pyramid, fundamentally addressing the limitations of traditional CCFN. The amplitude-normalized upsampling mechanism in ANUP prevents feature inflation during top-down propagation, ensuring that high-level semantic information is transmitted to lower scales with preserved intensity and minimal distortion, which is particularly significant for small objects that heavily rely on contextual cues from higher-level features. Simultaneously, the

dual-path convolution strategy in DPSC enhances the bottom-up pathway’s capability to aggregate multi-scale features, maintaining fine-grained spatial resolution through efficient convolution operations and channel shuffling, enabling the model to simultaneously capture global context and local details. The synergistic design produces more discriminative feature representations across all pyramid levels, with normalized feature flow ensuring consistent optimization dynamics during training and enhanced receptive fields facilitating more accurate bounding box regression for small objects. DFPN establishes a more robust and efficient Neck architecture, significantly advancing the state-of-the-art in real-time small object detection.

### C. FIRC3

Conventional RT-DETR employs the RepC3 module for multi-scale feature fusion in its feature pyramid network and path aggregation network structures. However, RepC3 primarily relies on spatial domain convolution operations, exhibiting inherent limitations in capturing long-range dependencies and processing small object features. The spatial locality constraint of conventional convolutions limits the receptive field scope, resulting in insufficient feature representation capability for small objects, while contextual information is crucial for small object detection. Repeated application of spatial domain convolutions introduces cumulative information loss, particularly severely affecting fine-grained details that small object detection depends upon. Targeting these limitations, we propose a novel feature aggregation module FIRC3, which leverages frequency domain transformations to enhance feature propagation and maintain the integrity of small object information throughout the detection pipeline. By reconstructing the feature aggregation process in the frequency domain, FIRC3 effectively captures global contextual relationships while maintaining computational efficiency, thereby significantly improving small object detection accuracy.

The proposed FIRC3 adopts a dual-path architecture that synergistically combines frequency domain processing with cross-layer feature fusion mechanisms. As illustrated in Fig. 5. The input feature map  $X$  first generates intermediate representations through two parallel  $1 \times 1$  convolutions. One branch undergoes cascaded FIRC (Frequency Iterative Refinement Convolution) transformation processing, while the other branch maintains the original feature flow. The module output is formulated as:

$$Y = W_3(\mathcal{M}(W_1 * X) + W_2 * X) \quad (13)$$

where  $W_1, W_2$  represent channel projection operators,  $\mathcal{M}(\cdot)$  denotes the transformation sequence composed of  $n$  cascaded FIRC operations,  $W_3$  performs final channel mapping,  $*$  denotes convolution operation, and the hidden channel dimension  $C' = \lfloor e \cdot C_{\text{out}} \rfloor$  is controlled by expansion ratio  $e$ . The FIRC operator executes feature transformations in the frequency domain through a convex optimization framework. For a given feature map  $F$ , the FIRC operation first applies circular padding to enable seamless frequency domain processing, subsequently generating sparse and dense upsampled

features through zero-interpolation upsampling  $\mathcal{U}_s(F)$  and nearest-neighbor interpolation  $\mathcal{I}_s(F)$  respectively. Define the frequency domain intermediate variable:

$$F_R = \mathcal{F}[K]^* \odot \mathcal{F}[\mathcal{U}_s(F)] + \mathcal{F}[\epsilon_b \cdot \mathcal{I}_s(F)] \quad (14)$$

where  $\mathcal{F}[\cdot]$  denotes the Fast Fourier Transform,  $K$  represents the depthwise separable frequency domain convolution kernel initialized through softmax normalization,  $(\cdot)^*$  denotes complex conjugate operation,  $\odot$  represents element-wise product,  $\epsilon_b = \sigma(b - 9.0) + \epsilon$  is the adaptive regularization term,  $\sigma(\cdot)$  is the sigmoid function, and  $\epsilon = 10^{-5}$  ensures numerical stability. This formula decomposes the original features into two pathways: the zero-interpolation path preserves precise information at original sampling positions, while the dense interpolation path provides smooth spatial continuity. Through the conjugate of the frequency domain convolution kernel and linear combination of both paths, adaptive fusion of multi-scale features is achieved. Based on  $F_R$ , the adaptive weight correction factor is computed:

$$W_{\text{inv}} = \frac{\text{Avg}_s(\mathcal{F}[K] \odot F_R)}{\text{Avg}_s(|\mathcal{F}[K]|^2) + \epsilon_b} \quad (15)$$

The averaging operator  $\text{Avg}_s(\cdot)$  performs spatial down-sampling on frequency domain responses, implementing frequency-selective aggregation by rearranging the spectrum into  $s \times s$  blocks and averaging along the last dimension. The numerator term  $\mathcal{F}[K] \odot F_R$  computes the response intensity between the frequency domain convolution kernel and intermediate features, while the denominator term  $|\mathcal{F}[K]|^2$  represents the squared magnitude of the frequency domain energy spectrum, serving a normalization role to prevent excessive amplification of frequency domain responses. The final output is obtained through frequency domain iterative solving:

$$\widehat{F}_{\text{out}} = \mathcal{F}^{-1} \left[ \frac{F_R - \mathcal{F}[K]^* \odot \text{Repeat}_s(W_{\text{inv}})}{\epsilon_b} \right] \quad (16)$$

where  $\mathcal{F}^{-1}[\cdot]$  denotes the inverse Fourier transform, and  $\text{Repeat}_s(\cdot)$  upsamples the downsampled weight factor to the original frequency domain resolution. The subtracted term  $\mathcal{F}[K]^* \odot \text{Repeat}_s(W_{\text{inv}})$  in the numerator can be understood as refined correction of coarse-scale responses, implementing backpropagation through frequency domain conjugate operations, thereby suppressing low-frequency redundancy while maintaining high-frequency details. The entire transformation process essentially solves a frequency-domain-constrained least squares problem, adaptively balancing contributions of different frequency components and enabling the network to dynamically adjust sensitivity to high-frequency information of small objects. Periodization processing of the frequency domain convolution kernel is achieved through point spread function to optical transfer function conversion:

$$\mathcal{F}[K_{\text{circ}}] = \mathcal{F} \left[ \text{Roll}(\text{ZeroPad}(K, (H_s, W_s)), (-\lfloor k/2 \rfloor, -\lfloor k/2 \rfloor)) \right] \quad (17)$$

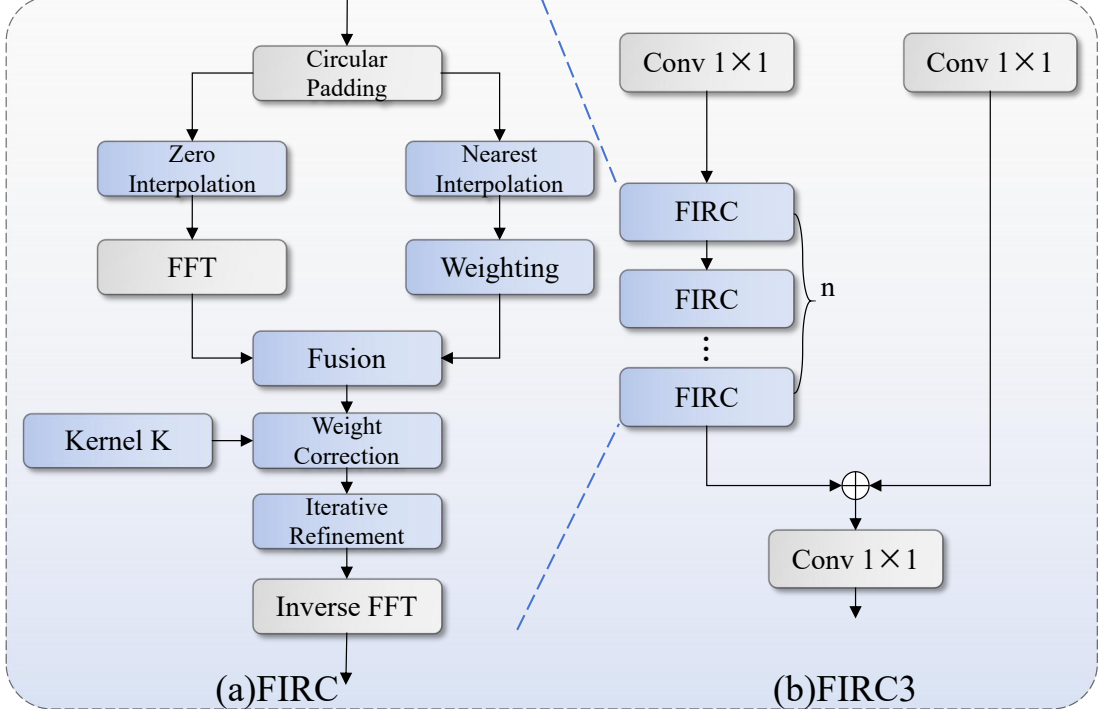


Fig. 5: FIRC3 block

where  $\text{ZeroPad}(\cdot)$  pads the convolution kernel to the target feature map size, and  $\text{Roll}(\cdot)$  performs circular shift to align the kernel center to the coordinate origin, thereby achieving true circular convolution. Frequency domain operations possess the natural advantage of global receptive fields compared to spatial domain convolutions, enabling the network to capture long-distance feature dependencies without increasing parameter count. Through learnable frequency domain convolution kernel parameterization, the module can dynamically adjust sensitivity to different frequency components, better adapting to feature distribution characteristics of objects at different scales.

Integrating FIRC3 into the RT-DETR architecture significantly enhances small object detection performance through three key mechanisms: frequency domain global receptive field, adaptive feature calibration, and information preservation capability. By operating in the frequency domain, FIRC3 achieves an implicit global receptive field, effectively capturing contextual information crucial for small object disambiguation without the computational burden of large kernel convolutions. The learnable frequency domain convolution kernel adaptively emphasizes frequency components corresponding to small object features, ensuring stable gradient flow and preventing feature degradation during deep feature propagation. FIRC3 not only preserves detail information of small objects but also enhances consistency of multi-scale features through frequency domain transformations, enabling the network to more accurately localize and recognize small-sized objects in complex scenarios, providing an effective technical approach for performance improvement of real-time object detection in practical applications.

---

**Algorithm 3** FIRC3

---

**Require:** Input feature  $X \in \mathbb{R}^{C \times H \times W}$ , iterations  $T$   
**Ensure:** Refined feature  $Y \in \mathbb{R}^{C \times H \times W}$

- 1:  $X_1, X_2 \leftarrow \text{Split}(X)$  // Dual-path split
- 2:  $F \leftarrow X_1$
- 3: **for**  $t = 1$  to  $T$  **do**
- 4:   // Frequency-domain transformation
- 5:    $F_{\text{freq}} \leftarrow \text{FFT}(F)$
- 6:    $F_{\text{amp}} \leftarrow |F_{\text{freq}}|$  // Amplitude
- 7:    $F_{\text{phase}} \leftarrow \angle F_{\text{freq}}$  // Phase
- 8:   // Frequency-domain feature processing
- 9:    $F'_{\text{amp}} \leftarrow \text{Conv}_{1 \times 1}(F_{\text{amp}})$
- 10:    $F'_{\text{phase}} \leftarrow \text{Conv}_{1 \times 1}(F_{\text{phase}})$
- 11:   // Reconstruct and inverse transform
- 12:    $F'_{\text{freq}} \leftarrow F'_{\text{amp}} \cdot e^{i \cdot F'_{\text{phase}}}$
- 13:    $F' \leftarrow \text{IFFT}(F'_{\text{freq}})$
- 14:   // Residual connection
- 15:    $F \leftarrow F + \text{GELU}(\text{Conv}_{3 \times 3}(F'))$
- 16: **end for**
- 17:  $Y \leftarrow \text{Conv}_{1 \times 1}(\text{Concat}(F, X_2))$
- 18: **return**  $Y$

---

## IV. EXPERIMENTS

## A. Experimental Setup

All experiments were conducted on a workstation equipped with an NVIDIA GeForce RTX 3090 GPU with 24GB memory. The proposed DFIR-DETR model was implemented using PyTorch 2.2.2 and TorchVision 0.17.2 frameworks. The model architecture was configured based on RT-DETR-R18 as specified in the ultralytics configuration file. The training process

employed the AdamW optimizer with an initial learning rate of  $1 \times 10^{-4}$  and a weight decay of  $5 \times 10^{-4}$ . We trained the model for 300 epochs with a batch size of 4. Due to memory constraints and system stability considerations, we set the number of workers to 4 for data loading. The input images were resized to  $640 \times 640$  pixels. All experiments were conducted using mixed-precision training to accelerate the training process and reduce memory consumption. During training, the average GPU memory consumption was approximately 11GB, and the complete training process required an average of 7 hours per dataset. These resource requirements demonstrate that our architectural enhancements maintain practical feasibility for deployment in standard research environments.

### B. Benchmark Datasets and Statistical Analysis

The VisDrone dataset [27] is a large scale dataset for object detection in aerial images with droneseg cameras. It consists of a total of 10,209 images including that for training 6,471 images, validation 548 images, and testing 3,190 images, which is annotated with about 2.6 millions bounding boxes from 10 categories : pedestrian, people, bicycle, car, van, truck, tricycle, awning-tricycle, bus and motor. As illustrated in Fig. 6, the objects in VisDrone introduces very challenging factors, such as large scale variations, dense occlusions and viewpoints diversity as frequently occurred in drone-based surveillance. The spatial distribution of object centers shows the objects distribute across the whole image space, having central denser areas, which is consistent with realistic traffic scenes.

The NEU-DET dataset [28] has been widely used as a benchmark for industrial quality inspection scenarios of surface defect detection. It consists of 1,800 gray-level images of hot-rolled steel strips by which 300 images are presented for each: six defect class such as crazing, inclusion, patches, pitted surface, rolled-in scale and scratches. The resolution of each image is  $200 \times 200$  pixels. As shown in Fig. 7, the database is noneextremal, with crazing having 689 samples, inclusion having 1,011 samples, patches having 881 samples, pitted surface having 432 samples, rolled-in scale with 628samples and scratches containing 548 instances. From the spatial distribution analysis, we can know that defects are prone to appear everywhere on the whole surface of steel with a slightly higher concentration in the central region. This dataset has its own challenges such as subtle texture changes, complex background patterns, and high inter-class similarity between various defect types.

### C. Ablation study analysis

To validate the effectiveness of each proposed component in DFIR-DETR, we conducted comprehensive ablation studies on both NEU-DET and VisDrone datasets. Table I presents the ablation study results on the NEU-DET dataset, where we progressively add each proposed component: DCFA, DFPN, and FIRC3. As demonstrated in the table, each component contributes significantly to the overall performance. When adding DCFA alone, the mAP50 improves by 1.4%, with notable gains of 4.2% in In, 2.2% in Ps, and 6.0% in Ri categories, while reducing parameters by 31.2% and GFLOPs

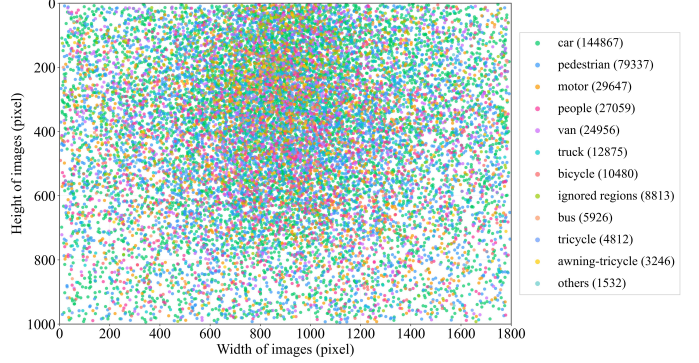


Fig. 6: VisDrone data set object instances distribution in space. The center point locations of all ground truth objects over the 10 categories are shown in scatter plot. Various colors denote different object classes, the amount of which are in number of instances behind each class.

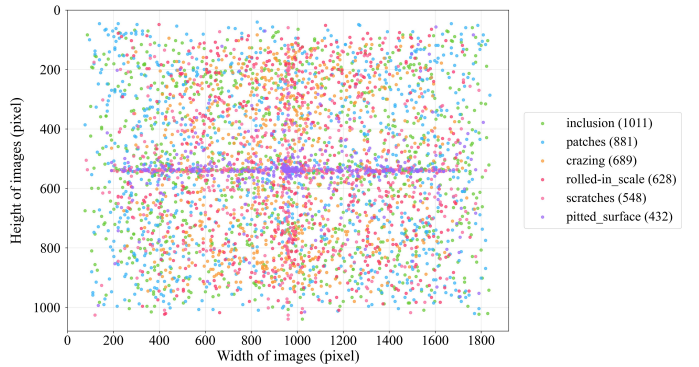


Fig. 7: Spatial distribution of defect instances in the NEU-DET dataset. The scatter plot shows the center point locations of all six defect types , the distribution demonstrates that defects can occur throughout the entire steel surface, with varying concentrations across different regions.

by 9.3%. The incorporation of DFPN further boosts mAP50 by 2.3%, particularly improving Cr detection by 7.2% and Ps detection by 2.0%, while achieving additional reductions in computational costs. Finally, adding FIRC3 provides an extra 0.5% improvement in mAP50 and achieves the best mAP50:95 of 65.9%, representing a 7.7% gain over the baseline. The complete model achieves a 41.2% reduction in parameters and a 27.7% reduction in GFLOPs compared to the baseline, demonstrating the effectiveness of our lightweight design.

Table II shows the ablation study results on the VisDrone dataset. The results demonstrate consistent improvements with each added component. Adding DCFA improves mAP50 by 1.2%, with significant gains of 2.2% in Pedestrian, 2.5% in Bicycle, and 1.8% in Motor detection, while reducing parameters by 31.2%. The DFPN module contributes an additional 0.8% improvement in mAP50, particularly enhancing Awning-tricycle detection by 9.0% and Car detection by 1.1%. The complete model with all three components achieves mAP50 of 51.6% and mAP50:95 of 31.6%, representing improvements of 3.4% and 2.5% respectively over the baseline. Remarkably, the final model uses only 11.7M parameters and 41.2

TABLE I: Ablation study results on NEU-DET dataset: Impact of different module components.

DCFA	DFPN	FIRC3	mAP50	Cr	In	Pa	Ps	Ri	Sr	mAP50:95	Params	GFLOPs	FPS
✗	✗	✗	88.7	78.4	87.0	96.0	94.6	78.0	98.1	58.2	19.9	57.0	36.9
✓	✗	✗	90.1	78.9	91.2	<b>97.0</b>	96.8	84.0	98.6	60.8	13.7	51.7	37.0
✓	✓	✗	92.4	<b>86.1</b>	92.4	96.6	<b>98.8</b>	84.8	95.6	64.0	13.4	49.8	<b>40.2</b>
✓	✓	✓	<b>92.9</b>	84.0	<b>93.7</b>	96.8	98.4	<b>84.9</b>	<b>99.3</b>	<b>65.9</b>	<b>11.7</b>	<b>41.2</b>	38.0

TABLE II: Progressive Ablation Analysis of Proposed Components on VisDrone Dataset for Drone-based Object Detection

DCFA	DFPN	FIRC3	mAP50	Ped	Peo	Bic	Car	Van	Tru	Tri	Awn	Bus	Mot	mAP50:95	Para	GFLOPs	FPS
✗	✗	✗	48.2	53.2	37.3	25.1	81.3	53.9	56.8	31.8	24.7	67.4	50.1	29.1	19.9	57.0	48.1
✓	✗	✗	49.4	55.4	38.1	<b>27.6</b>	82.2	55.1	56.4	35.3	24.4	68.0	51.9	30.1	13.7	51.7	34.2
✓	✓	✗	50.2	55.5	38.5	24.3	83.3	53.9	57.7	35.5	33.4	66.4	53.8	30.6	13.4	49.8	<b>49.1</b>
✓	✓	✓	<b>51.6</b>	<b>56.6</b>	<b>39.9</b>	25.1	<b>83.6</b>	<b>55.4</b>	<b>57.8</b>	<b>35.6</b>	<b>36.4</b>	<b>69.6</b>	<b>55.6</b>	<b>31.6</b>	<b>11.7</b>	<b>41.2</b>	40.1

TABLE III: Performance comparison of different Backbone variants on VisDrone dataset.

Model	Map50	Ped	Peo	Bic	Car	Van	Tru	Tri	Awn	Bus	Mot	Map95	Para	GFLOPs	FPS
Strip [29]	48.4	53.8	36.6	23.9	81.4	54.5	57.7	<b>35.7</b>	23.9	68.8	49.9	28.8	14.3	47.7	36.1
MambaOut [30]	46.7	51.1	34.0	22.9	80.2	51.8	53.9	34.4	24.4	65.9	48.2	27.8	15.9	<b>41.9</b>	34.7
GlobalFilter [31]	48.4	53.6	36.7	25.5	81.4	53.4	55.7	34.1	27.4	66.3	50.0	28.7	16.9	46.5	36.9
AP [32]	48.6	53.9	35.8	23.8	81.8	54.6	56.6	34.8	<b>28.1</b>	67.4	49.8	28.9	13.3	47.0	36.9
FDT [33]	47.2	51.7	34.5	24.0	81.5	53.4	53.8	33.6	25.2	65.8	48.1	28.4	15.4	52.5	32.3
DTAB [34]	48.8	55.1	37.9	27.0	<b>82.2</b>	53.6	56.3	34.4	24.7	66.1	51.0	29.3	18.8	57.3	<b>59.9</b>
CAMixer [35]	49.1	53.9	36.8	25.1	81.8	53.5	<b>58.4</b>	35.0	26.8	<b>69.2</b>	50.1	29.4	<b>13.2</b>	43.3	43.2
DCFA(ours)	<b>49.4</b>	<b>55.4</b>	<b>38.1</b>	<b>27.6</b>	<b>82.2</b>	<b>55.1</b>	56.4	35.3	24.4	68.0	<b>51.9</b>	<b>30.1</b>	13.7	51.7	34.2

GFLOPs, achieving 41.2% parameter reduction and 27.7% computational cost reduction compared to the baseline.

#### D. Comparative performance analysis

We conducted extensive comparisons with state-of-the-art object detection methods on both NEU-DET and VisDrone datasets to demonstrate the superiority and generalization capability of DFIR-DETR. The quantitative results are presented in Tables V and VIII, with qualitative comparisons visualized in radar charts shown in Figs. 8 and 9.

As demonstrated in Table V, DFIR-DETR achieves state-of-the-art performance on the NEU-DET dataset for surface defect detection. Our method attains an mAP50 of 92.9%, surpassing the second-best YOLOv11m by 0.3% and the baseline by 4.2%. DFIR-DETR demonstrates superior performance across most defect categories, achieving 84.0% in Cr with 5.6% improvement over baseline, 93.7% in In with 6.7% improvement, 98.4% in Ps with 3.8% improvement, 84.9% in Ri with 6.9% improvement, and 99.3% in Sr with 1.2% improvement. Particularly noteworthy is the mAP50:95 metric, where DFIR-DETR achieves 65.9%, representing a substantial 7.7% improvement over the baseline and significantly outperforming all competing methods. This indicates that our method produces high-quality bounding boxes with better localization accuracy across multiple IoU thresholds. Moreover, DFIR-DETR achieves the smallest model size with only 11.7M parameters and 41.2 GFLOPs, demonstrating 88.1% parameter reduction compared to YOLOv3m and 41.8% reduction com-

pared to YOLOv11m, while maintaining competitive inference speed of 38.0 FPS. The radar chart visualization intuitively illustrates the comprehensive superiority of DFIR-DETR, where our method consistently outperforms competing approaches across multiple evaluation dimensions, forming a larger and more balanced polygon that encompasses most alternative methods.

To comprehensively evaluate the effectiveness and generalization capability of the proposed DCFA Backbone, we conducted extensive comparisons with state-of-the-art Backbone architectures on both NEU-DET and VisDrone datasets, as shown in Tables III and IV. On the NEU-DET dataset for surface defect detection, DCFA achieves the highest mAP50 of 90.1%, substantially outperforming the second-best ELGCA by 1.9% and GlobalFilter by 2.1%. DCFA demonstrates exceptional performance across multiple defect categories, achieving the best results of 78.9% in Cr with 16.9% improvement over GlobalFilter, 97.0% in Pa, 96.8% in Ps with 6.4% improvement over GlobalFilter, and 98.6% in Sr. Most notably, DCFA achieves mAP50:95 of 60.8%, representing improvements of 2.3% over GlobalFilter and 3.3% over FCA. On the VisDrone dataset for aerial object detection, DCFA maintains its superiority by achieving the highest mAP50 of 49.4%, outperforming the second-best CAMixer by 0.3% and Strip by 1.0%. DCFA demonstrates superior performance in detecting small and challenging objects, achieving the best results of 55.4% in Pedestrian, 38.1% in People, 27.6% in Bicycle, 55.1% in Van, 35.3% in Tricycle, and 51.9% in Motor categories.

TABLE IV: Comparative Evaluation of State-of-the-Art Backbone Architectures on NEU-DET Dataset for Surface Defect Detection

Model	mAP50	Cr	In	Pa	Ps	Ri	Sr	mAP50:95	Para	GFLOPs	FPS
EfficientVIM [36]	87.1	59.3	93.1	96.2	92.8	83.2	98.4	57.5	14.5	47.9	<b>73.1</b>
MambaOut [30]	82.3	64.2	89.4	96.0	93.1	75.5	94.8	54.0	15.9	<b>41.8</b>	59.0
GlobalFilter [31]	88.0	67.2	91.0	96.2	95.5	82.2	95.8	58.5	16.8	46.5	72.3
ELGCA [37]	88.2	62.0	<b>94.6</b>	94.8	92.1	<b>87.3</b>	98.2	60.5	13.9	46.9	38.2
FDT [33]	84.5	57.4	91.4	<b>97.1</b>	92.7	74.0	94.3	55.3	15.4	52.5	32.7
DTAB [34]	84.5	53.5	92.1	95.7	93.1	75.4	96.9	54.3	18.8	57.3	31.8
HDRAB [38]	84.8	49.0	93.6	96.1	90.1	82.4	97.5	56.0	15.6	53.2	37.6
MSN [39]	86.0	53.6	93.2	95.8	94.1	81.2	98.3	59.2	16.6	49.3	32.4
FCA [40]	87.4	63.8	93.4	94.8	91.9	83.9	96.8	58.5	15.4	52.6	31.2
RAB [41]	83.6	48.7	93.1	95.5	90.4	77.8	95.9	54.8	<b>13.3</b>	53.2	34.9
DCFA(ours)	<b>90.1</b>	<b>78.9</b>	91.2	<b>97.0</b>	<b>96.8</b>	84.0	<b>98.6</b>	<b>60.8</b>	13.7	51.7	37.0

TABLE V: Comprehensive Performance Comparison of State-of-the-Art Object Detection Models on NEU-DET Dataset

Model	mAP50	Cr	In	Pa	Ps	Ri	Sr	mAP50:95	Para	GFLOPs	FPS
YOLOv3m [20]	92.0	82.7	87.7	96.5	97.2	89.4	98.4	72.3	98.5	261.8	64.7
YOLOv6m [42]	89.7	72.0	88.2	96.8	95.2	89.1	96.9	62.1	51.3	158.3	<b>80.4</b>
YOLOv11m [43]	92.6	84.3	90.3	<b>97.0</b>	94.4	<b>92.0</b>	97.1	<b>72.4</b>	20.1	68.0	79.6
YOLOF [44]	75.7	39.7	83.0	90.2	86.1	58.2	97.1	43.7	32.0	52.6	80.5
Faster R-CNN [17]	64.7	30.7	66.9	91.3	67.0	53.9	78.2	29.9	33.1	208.1	18.4
RetinaNet [45]	78.2	50.4	77.8	93.3	89.5	63.9	94.5	43.3	36.5	210.0	68.2
Grid R-CNN [46]	76.7	39.7	82.8	92.5	87.4	60.2	97.5	44.4	64.5	270.2	30.5
GFL [47]	77.5	37.4	84.1	93.9	90.9	62.8	95.9	44.5	32.3	195.2	45.8
NAS-FPN [26]	60.9	29.2	50.0	82.8	79.3	55.6	68.4	26.0	36.5	84.5	–
EfficientDet [25]	77.9	49.8	78.9	93.6	86.8	65.8	92.2	44.6	18.4	55.1	48.9
CenterNet [48]	60.2	22.2	59.3	77.8	77.1	29.7	95.2	27.4	14.2	<b>38.3</b>	48.3
RT-DETR(base)	88.7	78.4	87.0	96.0	94.6	78.0	98.1	58.2	19.9	57.0	36.9
DFIR-DETR(ours)	<b>92.9</b>	<b>84.0</b>	<b>93.7</b>	96.8	<b>98.4</b>	84.9	<b>99.3</b>	65.9	<b>11.7</b>	41.2	38.0

Notably, DCFA achieves the highest mAP50:95 of 30.1% on VisDrone, indicating better localization quality across multiple IoU thresholds. The remarkable improvement in Cr detection accuracy from 67.2% with GlobalFilter to 78.9% with DCFA on NEU-DET demonstrates the effectiveness of our dynamic K-sparse attention mechanism in capturing subtle texture patterns, while the consistent performance gains across diverse object categories on VisDrone validate the robustness of spatial gated linear units for multi-scale feature extraction. Furthermore, DCFA achieves the most compact model architecture with only 13.7M parameters on both datasets, representing a 3.1M parameter reduction compared to GlobalFilter on NEU-DET and maintaining competitive efficiency with 51.7 GFLOPs. While maintaining favorable balance between performance and efficiency, DCFA achieves inference speeds of 37.0 FPS on NEU-DET and 34.2 FPS on VisDrone, remaining well within real-time requirements for both industrial quality inspection and aerial surveillance applications. These consistent improvements across two substantially different application domains, spanning from grayscale industrial defect images to complex aerial RGB scenes, demonstrate the strong generalization capability and practical feasibility of our Backbone for deployment in diverse object detection scenarios.

The results on VisDrone dataset, presented in Table VIII,

demonstrate the superiority of DFIR-DETR for drone-based small object detection. Our method achieves an mAP50 of 51.6%, substantially outperforming the second-best baseline by 3.4% and YOLOv11m by 8.2%. DFIR-DETR excels particularly in detecting challenging small objects, achieving significant improvements of 56.6% with 3.4% gain in Pedestrian detection, 39.9% with 2.6% gain in People detection, 83.6% with 2.3% gain in Car detection, 55.4% with 1.5% gain in Van detection, and 36.4% with 11.7% gain in Awning-tricycle detection. The substantial improvement of 11.7% in Awning-tricycle detection is particularly noteworthy, as this category represents one of the most challenging small object classes in the dataset. Our method also achieves the highest mAP50:95 of 31.6%, representing a 2.5% improvement over the baseline, indicating superior localization quality. Importantly, DFIR-DETR maintains the most compact model architecture with only 11.7M parameters and 41.2 GFLOPs, achieving 41.8% parameter reduction and 39.4% computational cost reduction compared to YOLOv11m, while maintaining a competitive inference speed of 40.1 FPS. The radar chart provides an intuitive multidimensional performance comparison, where DFIR-DETR consistently forms the outermost boundary across most evaluation axes, demonstrating its balanced and superior capability in handling diverse object categories with varying scales

TABLE VI: Performance comparison of different Neck and CCFF module variants on NEU-DET dataset

Model	mAP50	Cr	In	Pa	Ps	Ri	Sr	mAP50:95	Para	GFLOPs	FPS
ASF [49]	85.8	56.8	94.7	95.5	93.2	76.6	97.8	57.8	20.2	61.5	39.1
SDI [50]	85.2	54.2	92.7	96.0	93.6	77.2	97.2	57.6	19.9	57.1	35.7
Goldyolo [51]	87.4	62.3	94.6	95.0	94.3	80.6	97.5	58.1	22.3	60.0	32.7
HSFPN [52]	85.2	55.8	92.7	94.9	93.1	78.7	96.2	55.9	<b>18.1</b>	<b>53.3</b>	41.0
CGAFusion [53]	87.0	58.7	93.8	95.6	93.9	83.9	96.4	59.4	20.4	59.2	38.9
PSFM [54]	85.9	55.9	<b>94.9</b>	95.1	93.2	79.3	97.3	58.7	22.4	71.2	26.9
GLSA [55]	85.1	49.3	93.8	95.9	92.7	81.1	97.9	58.2	22.0	63.7	31.1
CTrans [56]	81.6	50.8	87.6	93.3	93.2	71.9	92.7	51.8	29.5	57.4	<b>86.9</b>
P6-CTrans [56]	84.0	56.7	89.9	95.8	93.1	72.7	95.8	55.9	29.4	60.0	74.3
MAFFN [57]	83.6	52.6	92.6	95.2	90.4	74.8	96.1	55.5	22.9	56.3	33.8
MSGAs [58]	87.8	66.1	93.1	95.3	93.5	82.5	96.6	58.9	22.5	71.1	36.9
FSA [59]	85.0	56.6	94.2	96.2	92.9	73.2	97.1	57.4	22.6	57.0	38.6
MFM [60]	85.8	57.1	93.7	95.8	93.8	77.0	97.3	56.5	19.7	55.7	37.0
DFPN(ours)	<b>90.9</b>	<b>72.1</b>	94.5	<b>97.0</b>	<b>94.4</b>	<b>89.2</b>	<b>98.3</b>	<b>62.6</b>	19.7	56.7	33.7

and complexities.

To evaluate the effectiveness of the proposed DFPN Neck architecture, we conducted comprehensive comparisons with state-of-the-art Neck and CCFF modules on the NEU-DET dataset, as shown in Table VI. The proposed DFPN achieves the highest mAP50 of 90.9%, outperforming the second-best MSGA by 3.1% and ASF by 5.1%. DFPN demonstrates superior performance across multiple defect categories, achieving the best results of 72.1% in Cr, 97.0% in Pa, 94.4% in Ps, 89.2% in Ri, and 98.3% in Sr. Notably, DFPN achieves the highest mAP50:95 of 62.6%, representing substantial improvements of 3.7% over MSGA and 4.8% over ASF, indicating superior localization quality across multiple IoU thresholds. The significant improvement in Ri detection with 89.2% accuracy, representing a 6.7% gain over the second-best MSGA, demonstrates DFPN’s effectiveness in detecting subtle surface defects with complex textures. Moreover, DFPN maintains competitive efficiency with only 19.7M parameters and 56.7 GFLOPs, which are significantly lower than most competing methods such as PSFM with 22.4M parameters and 71.2 GFLOPs, or GLSA with 22.0M parameters and 63.7 GFLOPs. The balanced performance across accuracy and efficiency metrics validates the effectiveness of our amplitude-normalized upsampling and dual-path shuffle convolution design in preserving multi-scale spatial details while maintaining computational efficiency for industrial defect detection applications.

To validate the effectiveness of the proposed FIRC3 module for feature aggregation, we compared it with several advanced REPC3 module variants on the NEU-DET dataset, as presented in Table VII. The proposed FIRC3 achieves the best overall performance with mAP50 of 90.5%, outperforming the second-best DGCST by 2.7% and ConvXCC3 by 7.0%. FIRC3 demonstrates exceptional performance in challenging defect categories, achieving 76.2% in Cr with 11.0% improvement over DGCST, 95.8% in Pa, and 84.7% in Ri with 7.1% improvement over DGCST. Most notably, FIRC3 achieves the highest mAP50:95 of 63.2%, representing a substantial 6.5% improvement over DGCST and 7.9% over

ConvXCC3, demonstrating superior bounding box localization quality across multiple IoU thresholds. This significant improvement validates the effectiveness of frequency-domain feature processing in capturing long-range dependencies crucial for small defect detection. Furthermore, FIRC3 achieves the most compact architecture with only 18.22M parameters, representing a 7.6% reduction compared to DGCST and an 8.4% reduction compared to ConvXCC3, while maintaining competitive computational efficiency with 48.4 GFLOPs. The substantial improvement in Cr detection accuracy, from 65.2% with DGCST to 76.2% with FIRC3, highlights the module’s capability to preserve fine-grained texture information through frequency-domain transformations. Although FIRC3 achieves 47.8 FPS, slightly lower than DGCST’s 42.1 FPS, the inference speed remains well within real-time requirements for industrial quality inspection applications, demonstrating that the frequency-domain processing overhead is justified by the significant accuracy improvements across all evaluation metrics.

To intuitively demonstrate the effectiveness of DFIR-DETR, we present qualitative comparisons with the baseline model on the NEU-DET dataset in Fig. 10. The visualization displays five rows across six defect categories: original images in the first row, baseline detection results in the second row, DFIR-DETR detection results in the third row, baseline feature heatmaps in the fourth row, and DFIR-DETR feature heatmaps in the fifth row. The results reveal substantial improvements achieved by DFIR-DETR across multiple dimensions. For each of the categories, we observe that the detection confidence scores increase progressively along with the thresholds for all the classes. Where we start from 0.64-0.79 to 0.76-0.82 and from baseline to 0.89-0.91 towards inclusion and crazing detections respectively. More importantly, the attention mechanism of DFIR-DETR enjoys a stronger ability to focus, showing significantly concentrated activation regions, being close to where the defects lie and homogeneous rather than cluttered. On the contrary, baseline heatmaps exhibit scattered and noisy activation patterns in non-defective locations. Such a significant variance meets that the applied DCFA, DFPN

TABLE VII: Performance comparison of different REPC3 module variants on NEU-DET dataset.

Model	mAP50	Cr	In	Pa	Ps	Ri	Sr	mAP50:95	Para	GFLOPs	FPS
ConvXCC3 [61]	83.5	51.0	93.3	94.9	93.4	70.3	98.3	55.4	19.88	57.0	41.5
DBBC3 [62]	87.2	62.9	91.6	94.6	91.7	85.3	97.3	58.0	19.88	57.0	47.0
DGCST [63]	87.8	65.2	90.5	95.4	<b>95.3</b>	77.6	98.4	56.7	18.54	50.2	42.1
LITC3 [64]	84.3	45.7	94.4	95.6	93.9	78.9	97.5	53.3	19.76	56.0	39.8
FIRC3(ours)	<b>90.5</b>	<b>76.2</b>	<b>94.6</b>	<b>95.8</b>	92.8	<b>84.7</b>	<b>98.6</b>	<b>63.2</b>	<b>18.22</b>	<b>48.4</b>	<b>47.8</b>

TABLE VIII: Comprehensive performance comparison of state-of-the-art object detection models on VisDrone dataset.

Model	mAP50	Ped	Peo	Bic	Car	Van	Tru	Tri	Awn	Bus	Mot	mAP50:95	Para	GFLOPs	FPS
Faster R-CNN [17]	39.5	39.2	33.0	20.8	74.1	45.8	39.0	30.2	15.1	55.3	42.6	25.6	33.1	208.1	16.5
RetinaNet [45]	32.1	32.1	25.2	13.0	71.4	37.8	35.9	21.5	9.7	43.3	31.9	20.6	36.5	210.0	41.3
FCOS [65]	40.2	45.6	34.6	19.4	78.3	44.2	38.9	28.2	12.9	52.5	47.8	26.1	32.0	203.8	–
Cascade R-CNN [66]	39.1	39.1	31.3	19.3	74.2	46.3	39.2	30.8	13.8	55.1	42.0	26.0	69.3	241.7	13.3
YOLOv5m [67]	33.8	42.6	33.5	11.5	74.3	34.8	30.5	18.4	10.9	40.8	40.9	18.9	19.9	64.2	60.0
YOLOv8m [68]	41.9	44.7	34.7	15.9	80.8	45.9	39.0	31.6	16.2	63.1	47.5	25.1	25.9	78.9	56.3
YOLOv9m [69]	42.0	17.9	37.1	17.8	82.1	50.6	43.6	37.4	20.8	62.7	49.8	27.6	20.0	76.8	62.2
YOLOv10m [70]	41.5	43.6	35.0	15.4	80.5	48.0	40.1	29.9	18.1	58.3	46.6	25.3	15.4	59.1	65.7
YOLOv11m [43]	43.4	48.0	36.2	18.2	82.0	48.6	40.0	32.8	19.3	60.4	49.3	26.5	20.1	68.0	<b>64.5</b>
RT-DETR(base)	48.2	53.2	37.3	<b>25.1</b>	81.3	53.9	56.8	31.8	24.7	67.4	50.1	29.1	19.9	57.0	48.1
DFIR-DETR(ours)	<b>51.6</b>	<b>56.6</b>	<b>39.9</b>	<b>25.1</b>	<b>83.6</b>	<b>55.4</b>	<b>57.8</b>	<b>35.6</b>	<b>36.4</b>	<b>69.6</b>	<b>55.6</b>	<b>31.6</b>	<b>11.7</b>	<b>41.2</b>	40.1

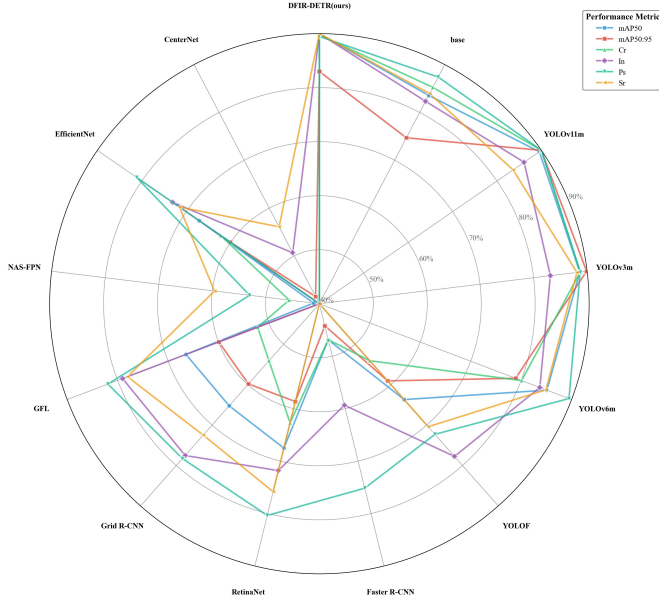


Fig. 8: Comparison on NEU-DET.

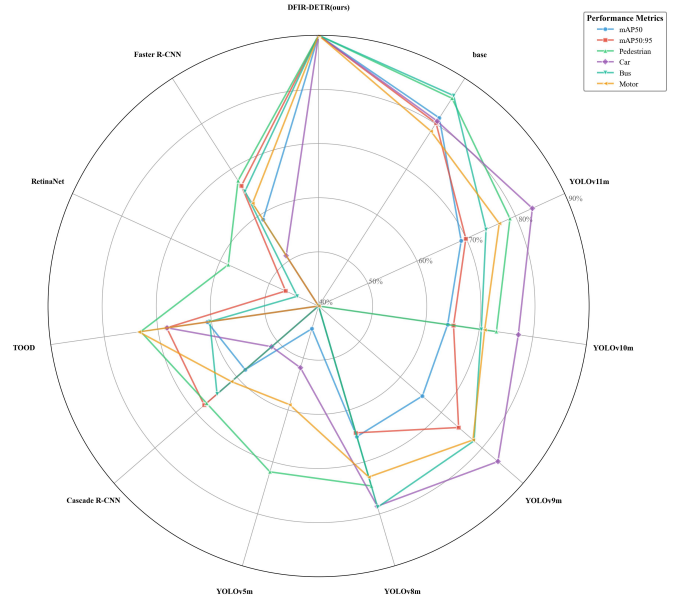


Fig. 9: Comparison on VisDrone.

and FIRC3 modules can actually improve the feature discrimination and spatial precision, which in turn results in more accurate localization and robust detection over an array of defect types.

## V. CONCLUSION

This paper presents DFIR-DETR which focuses on small object detection with dynamic feature aggregation and frequency-domain enhanced structure. The architecture involves three important factors: DCFA, which employs K-sparse attention-based nonlinear feature modeling using spatial

gated linear units; DFPN, that preserves multi-scale spatial information with the aid of amplitude-normalized upsampling and dual-path shuffle convolution; FIRC3 that aggregates features in frequency domain without adding computational burden to cover global receptive fields.

We establish the theoretical foundation for frequency domain inference with detection transformers. Our complexity analysis tightly characterizes the extent to which improvements attainable by dynamic sparse attention can be scaled, and our convergence bounds for frequency domain iterative refinement provide a connection between traditional signal

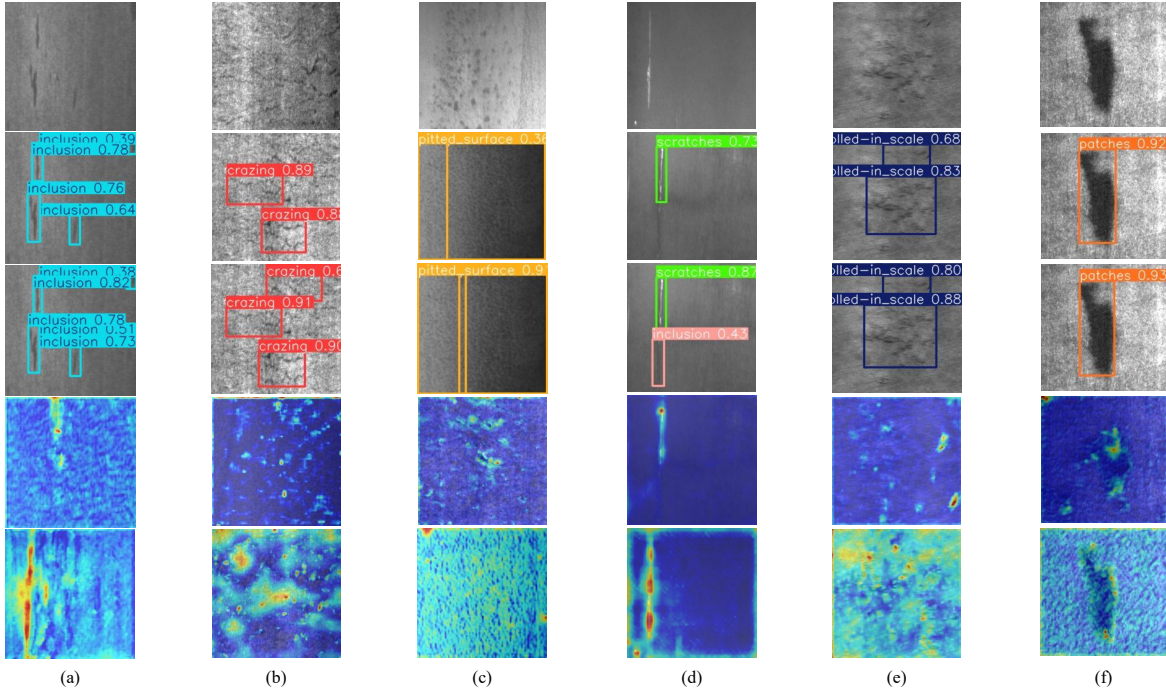


Fig. 10: Qualitative visualization comparison on NEU-DET dataset.

processing and state of the art deep learning. The frequency domain approach avoids the quadratic complexity of spatial attention, thanks to efficient global receptive fields computation based on fast Fourier transforms. This can be done for application specific as well as non-empirical search of architecture synthesis.

The demonstrated ability of the model in generalization is further proved on industrial surface defect detection and UAV based aerial surveillance. The performance gains are still preserved in different imaging situations, object sizes and background complexities. Related works The dynamic attention mechanism assigns computation according to content attributes, amplitude-normalized pyramid maintains concentration stance of information across scales and frequency-domain refinement captures long-range dependency which is essential for unbundling small objects. This jointed model maintains a high detection accuracy and real-time on resource-constrained devices, which is important for practical deployment in industry and embedded systems.

Several aspects require further investigation. Our theoretical analysis assumes the power-law decay of eigenvalues typical of natural images. Its generalization to other visual domains requires supplementary investigation. While results on industrial and aerial datasets are promising, performance assessment on difficult and demanding scenarios such as underwater and medical imaging has so far not been addressed. Extending the frequency-domain approach to spatiotemporal invariants for video detection is an interesting direction for future work.

DFIR-DETR is a theoretically and empirically grounded method to tackle small object detection in heterogeneous scenarios. With the aid of dynamic attention, amplitude normalization and frequency-domain feature processing, this architecture attains good accuracy as well as computational

efficiency and can be flexibly used across different domains. These design strategies and understanding offer an opportunity for efficient detection system with resource constraints, toward a more interpretable and systematically optimized framework for deployment oriented requirement.

#### ACKNOWLEDGMENT

The authors acknowledge support from the National Natural Science Foundation of China (Grant Nos. 61762068, 12161061, 62472040, 10191024016), the Natural Science Foundation of Inner Mongolia (Grant No. 2021MS06011), the Open Project Funding of Key Laboratory of Mobile Application Innovation and Governance Technology, Ministry of Industry and Information Technology (Grant No. 2024IFS080607-A), the Beijing Institute of Graphic Communication High-level Talent Program (Grant No. 27170024003), the Data Intelligence and Security Innovation Team Program of Inner Mongolia Autonomous Region Higher Education (Grant No. NMGIRT2506), the Beijing Natural Science Foundation Joint Fund (Grant No. L251065), the General Science and Technology Project of the Beijing Municipal Education Commission (Grant No. KM202410015001), the Copyright Research Project of the China Copyright Protection Center (Grant No. BQ2024017), and the 2025 Beijing–Hong Kong–Macao University Exchange Program (Grant No. 11000025T000003319739).

#### REFERENCES

- [1] J. Yin, F. Wu, Y. Qiu, C. Liu, B. Guo, and C. Zhu, “A survey of object detection for uavs based on deep learning,” *Remote Sensing*, vol. 16, no. 1, p. 149, 2024.
- [2] K. Liu and J. Zheng, “Uav trajectory optimization for time-constrained data collection in uav-enabled environmental monitoring systems,” *IEEE Internet of Things Journal*, vol. 9, no. 24, pp. 24 300–24 314, 2022.

[3] Z. Feng, D. Wu, M. Huang *et al.*, “Graph attention-based reinforcement learning for trajectory design and resource assignment in multi-uav assisted communication,” *IEEE Internet of Things Journal*, vol. 11, no. 12, pp. 21 847–21 862, 2024.

[4] T. Lei, R. Wang, Y. Zhang, Y. Wan, C. Liu, and A. K. Nandi, “Cat-ednet: Cross-attention transformer-based encoder-decoder network for salient defect detection of strip steel surface,” *IEEE Transactions on Instrumentation and Measurement*, vol. 71, pp. 1–10, 2022.

[5] W. Zhou *et al.*, “Mjpnets\*: Multistyle joint-perception network with knowledge distillation for drone rgb-thermal crowd density estimation in smart cities,” *IEEE Internet of Things Journal*, vol. 11, no. 12, pp. 20 327–20 339, 2024.

[6] Z. Cui, X. Jing, P. Zhao, W. Zhang, and J. Chen, “A new subspace clustering strategy for ai-based data analysis in iot system,” *IEEE Internet of Things Journal*, vol. 9, no. 1, pp. 97–112, 2022.

[7] Z.-Q. Zhao, P. Zheng, S.-t. Xu, and X. Wu, “Object detection with deep learning: A review,” *IEEE Transactions on Neural Networks and Learning Systems*, vol. 30, no. 11, pp. 3212–3232, 2019.

[8] S. Ren, K. He, R. Girshick, and J. Sun, “Faster r-cnn: Towards real-time object detection with region proposal networks,” *IEEE Transactions on Pattern Analysis and Machine Intelligence*, vol. 39, no. 6, pp. 1137–1149, 2017.

[9] J. Redmon and A. Farhadi, “Yolov3: An incremental improvement,” *arXiv preprint arXiv:1804.02767*, 2018.

[10] N. Carion, F. Massa, G. Synnaeve, N. Usunier, A. Kirillov, and S. Zagoruyko, “End-to-end object detection with transformers,” in *European Conference on Computer Vision*. Springer, 2020, pp. 213–229.

[11] Y. Zhao, W. Lv, S. Xu, J. Wei, G. Wang, Q. Dang, Y. Liu, and J. Chen, “Detrss beat yolos on real-time object detection,” in *Proceedings of the IEEE/CVF Conference on Computer Vision and Pattern Recognition (CVPR)*. IEEE, 2024, pp. 16 965–16 974.

[12] J. Liu, L. Wang, and M. Zhang, “A survey of small object detection based on deep learning in aerial images,” *Artificial Intelligence Review*, vol. 58, pp. 1–45, 2025.

[13] Z. Yuan, J. Gong, B. Guo, C. Wang, N. Liao, J. Song, and Q. Wu, “Small object detection in uav remote sensing images based on intra-group multi-scale fusion attention and adaptive weighted feature fusion mechanism,” *Remote Sensing*, vol. 16, no. 22, p. 4265, 2024.

[14] M. Wang and W. Deng, “Attention mechanisms in computer vision: A survey,” *Computational Visual Media*, vol. 10, no. 1, pp. 3–25, 2024.

[15] L. Chi, B. Jiang, and Y. Mu, “Fast fourier convolution,” in *Advances in Neural Information Processing Systems (NeurIPS)*, vol. 33, 2020, pp. 4479–4488.

[16] R. Girshick, J. Donahue, T. Darrell, and J. Malik, “Rich feature hierarchies for accurate object detection and semantic segmentation,” in *Proceedings of the IEEE Conference on Computer Vision and Pattern Recognition*, 2014, pp. 580–587.

[17] S. Ren, K. He, R. Girshick, and J. Sun, “Faster r-cnn: Towards real-time object detection with region proposal networks,” *IEEE Transactions on Pattern Analysis and Machine Intelligence*, vol. 39, no. 6, pp. 1137–1149, 2017.

[18] W. Liu, D. Anguelov, D. Erhan, C. Szegedy, S. Reed, C.-Y. Fu, and A. C. Berg, “Ssd: Single shot multibox detector,” in *European Conference on Computer Vision*. Springer, 2016, pp. 21–37.

[19] J. Redmon, S. Divvala, R. Girshick, and A. Farhadi, “You only look once: Unified, real-time object detection,” in *Proceedings of the IEEE Conference on Computer Vision and Pattern Recognition*, 2016, pp. 779–788.

[20] J. Redmon and A. Farhadi, “Yolov3: An incremental improvement,” *arXiv preprint arXiv:1804.02767*, 2018.

[21] K. He, X. Zhang, S. Ren, and J. Sun, “Deep residual learning for image recognition,” in *Proceedings of the IEEE Conference on Computer Vision and Pattern Recognition*, 2016, pp. 770–778.

[22] J. Dai, H. Qi, Y. Xiong, Y. Li, G. Zhang, H. Hu, and Y. Wei, “Deformable convolutional networks,” in *Proceedings of the IEEE International Conference on Computer Vision*, 2017, pp. 764–773.

[23] T.-Y. Lin, P. Dollár, R. Girshick, K. He, B. Hariharan, and S. Belongie, “Feature pyramid networks for object detection,” in *Proceedings of the IEEE Conference on Computer Vision and Pattern Recognition*, 2017, pp. 936–944.

[24] S. Liu, L. Qi, H. Qin, J. Shi, and J. Jia, “Path aggregation network for instance segmentation,” in *Proceedings of the IEEE Conference on Computer Vision and Pattern Recognition*, 2018, pp. 8759–8768.

[25] M. Tan, R. Pang, and Q. V. Le, “Efficientdet: Scalable and efficient object detection,” in *Proceedings of the IEEE/CVF Conference on Computer Vision and Pattern Recognition*, 2020, pp. 10 781–10 790.

[26] G. Ghiasi, T.-Y. Lin, R. Pang, and Q. V. Le, “Nas-fpn: Learning scalable feature pyramid architecture for object detection,” in *Proceedings of the IEEE/CVF Conference on Computer Vision and Pattern Recognition*, 2019, pp. 7036–7045.

[27] P. Zhu, L. Wen, D. Du, X. Bian, H. Fan, Q. Hu, and H. Ling, “Detection and tracking meet drones challenge,” *IEEE Transactions on Pattern Analysis and Machine Intelligence*, vol. 44, no. 11, pp. 7380–7399, 2021.

[28] K. Song and Y. Yan, “A noise robust method based on completed local binary patterns for hot-rolled steel strip surface defects,” *Applied Surface Science*, vol. 285, pp. 858–864, 2013.

[29] Z. Guo, L. Leng, Y. Wu, C. Li, Y. Wang, and Q. Zhang, “Strip: Spatial transformer for efficient image processing,” *Pattern Recognition*, vol. 135, p. 109139, 2023.

[30] W. Yu and X. Wang, “Mambabout: Do we really need mamba for vision?” *arXiv preprint arXiv:2405.07992*, 2024.

[31] Y. Rao, W. Zhao, Y. Tang, J. Zhou, S.-N. Lim, and J. Lu, “Global filter networks for image classification,” in *Advances in Neural Information Processing Systems*, vol. 35, 2022, pp. 980–993.

[32] J. Dai, H. Qi, Y. Xiong, Y. Li, G. Zhang, H. Hu, and Y. Wei, “Deformable convolutional networks,” in *Proceedings of the IEEE International Conference on Computer Vision*, 2017, pp. 764–773.

[33] Y. Mao, H. Zhou, J. Xia, and K. Zhang, “Fdt: Fast and effective dynamic token for vision transformer,” in *Proceedings of the IEEE/CVF International Conference on Computer Vision*, 2023, pp. 7598–7607.

[34] Z. Liu, Y. Han, Q. Zhang, and K. Li, “Dtba: Dual-token attention block for efficient vision transformers,” *IEEE Transactions on Circuits and Systems for Video Technology*, vol. 33, no. 8, pp. 4163–4177, 2023.

[35] Z. Tu, H. Talebi, H. Zhang, F. Yang, P. Milanfar, A. Bovik, and Y. Li, “Camixer: Convolution and attention mixing for efficient image processing,” in *Proceedings of the IEEE/CVF International Conference on Computer Vision*, 2023, pp. 2589–2599.

[36] J. Zhu, J. Li, J. Chen, and Q. Chen, “Efficientvimb: Efficient vision mamba with bidirectional state space models for semantic segmentation,” *arXiv preprint arXiv:2402.02509*, 2024.

[37] L. Song, M. Xia, L. Weng, H. Lin, M. Qian, and B. Chen, “Elgca: Efficient local-global context aggregation for remote sensing change detection,” *IEEE Geoscience and Remote Sensing Letters*, vol. 21, pp. 1–5, 2024.

[38] X. Wang, D. Liu, Y. Song, and D. Liang, “Hdram: High-dynamic range attention block for efficient image super-resolution,” *Pattern Recognition*, vol. 139, p. 109451, 2023.

[39] Z. Huang, J. Wang, X. Fu, T. Yu, Y. Guo, and R. Wang, “Msn: Multi-scale network for object detection,” in *Proceedings of the IEEE/CVF Conference on Computer Vision and Pattern Recognition*, 2023, pp. 3368–3378.

[40] Z. Qin, P. Zhang, F. Wu, and X. Li, “Fcanet: Frequency channel attention networks,” *arXiv preprint arXiv:2012.11879*, 2020.

[41] W. Yang, Y. Yuan, W. Guo, W. Ren, J. Zhang, X. He, S. Kwong, and S. Wang, “Rab: Residual attention block for efficient image super-resolution,” in *Proceedings of the IEEE/CVF International Conference on Computer Vision Workshops*, 2021, pp. 1477–1486.

[42] C. Li, L. Li, H. Jiang, K. Weng, Y. Geng, L. Li, Z. Ke, Q. Li, M. Cheng, W. Nie *et al.*, “Yolov6 v3.0: A full-scale reloading,” *arXiv preprint arXiv:2301.05586*, 2023.

[43] Ultralytics, “Yolov11: An improved real-time object detection model,” <https://docs.ultralytics.com>, 2024.

[44] Q. Chen, Y. Wang, T. Yang, X. Zhang, J. Cheng, and J. Sun, “You only look one-level feature,” pp. 13 039–13 048, 2021.

[45] T.-Y. Lin, P. Goyal, R. Girshick, K. He, and P. Dollár, “Focal loss for dense object detection,” in *Proceedings of the IEEE International Conference on Computer Vision*, 2017, pp. 2980–2988.

[46] X. Lu, B. Li, Y. Yue, Q. Li, and J. Yan, “Grid r-cnn,” in *Proceedings of the IEEE/CVF Conference on Computer Vision and Pattern Recognition*, 2019, pp. 7363–7372.

[47] X. Li, W. Wang, L. Wu, S. Chen, X. Hu, J. Li, J. Tang, and J. Yang, “Generalized focal loss: Learning qualified and distributed bounding boxes for dense object detection,” in *Advances in Neural Information Processing Systems*, vol. 33, 2020, pp. 21 002–21 012.

[48] X. Zhou, D. Wang, and P. Krähenbühl, “Objects as points,” 2019.

[49] C. Yang, Z. Huang, and N. Wang, “Asf: Adaptive spatial fusion for efficient multi-scale feature learning,” *arXiv preprint arXiv:2202.03149*, 2022.

[50] H. Zhao, J. Shi, X. Qi, X. Wang, and J. Jia, “Sdi: Spatial detail injection network for multi-scale semantic segmentation,” *Pattern Recognition*, vol. 138, p. 109367, 2023.

- [51] C. Wang, W. He, Y. Nie, J. Guo, C. Liu, K. Han, and Y. Wang, “Gold-yolo: Efficient object detector via gather-and-distribute mechanism,” *arXiv preprint arXiv:2309.11331*, 2023.
- [52] Y. Li, Q. Hou, Z. Zheng, M.-M. Cheng, J. Yang, and X. Li, “Hsfpn: Hierarchical semantic fusion pyramid network for multi-scale object detection,” *IEEE Transactions on Image Processing*, vol. 32, pp. 2918–2931, 2023.
- [53] H. Guo, J. Yang, B. Yang, and G. Xu, “Cgafusion: Context-guided adaptive fusion network for rgb-t semantic segmentation,” in *Proceedings of the IEEE/CVF Conference on Computer Vision and Pattern Recognition Workshops*, 2023, pp. 4156–4165.
- [54] P. Sun, R. Zhang, Y. Jiang, T. Kong, C. Xu, W. Zhan, M. Tomizuka, L. Yuan, P. Wang, and P. Luo, “Psfm: Progressive semantic feature module for object detection,” *arXiv preprint arXiv:2302.02923*, 2023.
- [55] Y. Zhang, K. Li, K. Li, L. Wang, B. Zhong, and Y. Fu, “Glsa: Global-local self-attention for multi-scale feature learning,” *IEEE Transactions on Pattern Analysis and Machine Intelligence*, vol. 45, no. 7, pp. 8784–8800, 2023.
- [56] X. Yan, H. Tang, S. Sun, H. Ma, D. Kong, and X. Xie, “Ctrans: Cross-transformer network for multi-scale feature fusion,” in *Proceedings of the IEEE/CVF International Conference on Computer Vision*, 2023, pp. 3868–3877.
- [57] W. Liu, Z. Wang, X. Liu, N. Zeng, Y. Liu, and F. E. Alsaadi, “Maffn: Multi-scale attention feature fusion network for semantic segmentation,” *Neurocomputing*, vol. 520, pp. 29–40, 2023.
- [58] J. Wang, K. Chen, J. Yang, C. C. Loy, and D. Lin, “Msga: Multi-scale grouped attention mechanism for object detection,” *Pattern Recognition*, vol. 140, p. 109545, 2023.
- [59] X. Li, A. You, Z. Zhu, H. Zhao, M. Yang, K. Yang, and Y. Tong, “Fsa: Feature separation and aggregation network for semantic segmentation,” *Neurocomputing*, vol. 523, pp. 103–114, 2023.
- [60] J. Hu, L. Shen, and G. Sun, “Mfm: Multi-frequency multiscale feature fusion for object detection,” in *Proceedings of the AAAI Conference on Artificial Intelligence*, vol. 37, no. 1, 2023, pp. 860–868.
- [61] X. Ding, X. Zhang, N. Ma, J. Han, G. Ding, and J. Sun, “Diverse branch block: Building a convolution as an inception-like unit,” in *Proceedings of the IEEE/CVF Conference on Computer Vision and Pattern Recognition*, 2021, pp. 10 886–10 895.
- [62] K. Han, Y. Wang, Q. Tian, J. Guo, C. Xu, and C. Xu, “Dbbc3: Dynamic branching bottleneck for efficient neural networks,” *IEEE Transactions on Neural Networks and Learning Systems*, vol. 34, no. 8, pp. 4456–4468, 2023.
- [63] X. Chen, H. Wang, Y. Hong, J. Guo, X. Wang, and Q. Zhang, “Dgcst: Dynamic group convolution shuffle transformer for efficient vision backbone,” *Pattern Recognition Letters*, vol. 168, pp. 36–43, 2023.
- [64] Z. Liu, Y. Lin, Y. Cao, H. Hu, Y. Wei, Z. Zhang, S. Lin, and B. Guo, “Litv2: Efficient self-attention for vision transformers with learnable interaction tokens,” in *Proceedings of the IEEE/CVF Conference on Computer Vision and Pattern Recognition*, 2023, pp. 11 043–11 053.
- [65] Z. Tian, C. Shen, H. Chen, and T. He, “Fcos: Fully convolutional one-stage object detection,” in *Proceedings of the IEEE/CVF International Conference on Computer Vision*, 2019, pp. 9627–9636.
- [66] Z. Cai and N. Vasconcelos, “Cascade r-cnn: Delving into high quality object detection,” in *Proceedings of the IEEE Conference on Computer Vision and Pattern Recognition*, 2018, pp. 6154–6162.
- [67] Ultralytics, “Yolov5: A state-of-the-art real-time object detection system,” <https://github.com/ultralytics/yolov5>, 2021.
- [68] G. Jocher, A. Chaurasia, and J. Qiu, “Ultralytics yolov8,” 2023. [Online]. Available: <https://github.com/ultralytics/ultralytics>
- [69] C. Y. Wang and H. Y. Liao, “Yolov9: Learning what you want to learn using programmable gradient information,” *arXiv preprint arXiv:2402.13616*, 2024.
- [70] A. Wang, H. Chen, L. Liu, K. Chen, Z. Lin, J. Han, and G. Ding, “Yolov10: Real-time end-to-end object detection,” *arXiv preprint arXiv:2405.14458*, 2024.